EXPERIMENTAL AND NUMERICAL ANALYSIS OF MULTI-PASS WELDING

FELIX KOCH*, MARCO ENDERLEIN

Technische Universität Bergakademie Freiberg
Institute of Mechanics and Fluid Dynamics
Lampadiusstraße 4
09599 Freiberg (Germany)
*Corresponding author: Felix.Koch@imfd.tu-freiberg.de

Abstract

Numerical simulation is nowadays used as a primary design tool to assess welded joints within the scope of the optimization of welding procedures. The prediction of the temperature field is the basis of the computer aided assessment of welds. This paper introduces a calculation approach for the temperature field of multi-pass welding. Manual electric welding is modelled using the finite element method (FEM) within the software ABAQUS. A modification of the double-ellipsoidal Goldak heat source is implemented considering the effects of filler metal and slag. In order to increase the efficiency of multi-pass welding simulation the Goldak source is projected onto each bead contour. Welding experiments are carried out containing a manual surfacing. The computational results are validated with macro sections and thermocouple measurements.

Finally the calculated temperature field is in good agreement with the fusion line and heat-affected-zone obtained from the macro sections and also fits with the thermocouple measurement. The slag mainly influences the cooling velocity within the heat affected zone (HAZ) of the computation model.

Key words: multi-pass welding, heat source modelling, temperature field, filler metal, slag

1. INTRODUCTION

Welding is one of the most common techniques to assemble metal structures. When welding is applied to devices such as gas pipelines strong safety requirements must be met for the welded joints. For this purpose numerical welding simulation is an established method to predict the mechanical properties of the weld. In 2011 the first standard on the computer aided assessment of welds was published: "Numerical welding simulation – Execution and documentation" (DIN SPEC 32534-1).

The prediction of the welding temperature field is the basis of the computer aided assessment of welds. The quality of the thermal analysis is decisive

for the calculation of residual welding stresses and the prediction of the microstructure distribution. Therefore, the present paper focuses on the realistic computation of the temperature field during multi-pass welding. In accordance with the-state-of-the-art-technology the temperature field is calculated within a heat conduction model. For this procedure the heat input is defined by a power density distribution a so called heat source model. An overview of the commonly used heat source models is given by Lindgren (2007), Goldak and Akhlaghi (2005) and Radaj (1999). The Goldak heat source model is generally recommended for the simulation of manual electric welding (ibid.). Deng and Murakawa (2006) and Sabapathy et al. (2001) obtained realistic tem-

perature fields using this model and within the present paper the model is applied to compute manual multi-pass welding.

2. MODELLING ABSTRACTIONS

The interaction between the temperature field, the microstructure development and the mechanical stresses has to be analysed in order to assess welded joints. In the case of industrial applications the assessment is usually realized by a structural analysis within the so called classical computational welding mechanics, Lindgren (2007). Within the structural analysis the multi-physic of welding is reduced to a pure heat conduction problem. The computed temperature field is used to predict the development of microstructure and the thermal stresses via sequentially thermomechanical coupling, as shown in figure 1.
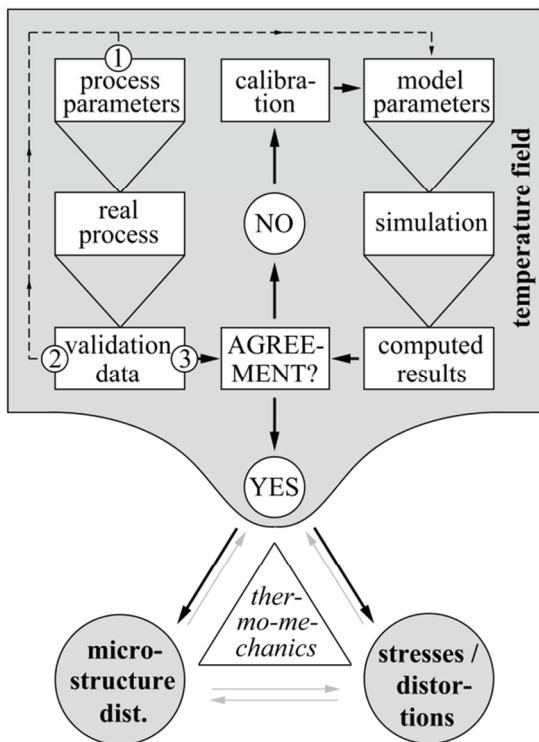
Fig. 1. *Thermo-mechanics and inverse modelling of heat transfer during welding (cp. Pittner et al. (2011) and Weiss et al. (2007), 1: known welding parameters, 2: bead shape geometry, 3: temperature field measurement)*

The heat input during welding is simplified using a so called equivalent heat source within the temperature field calculation. Such a heat source model contains a power density distribution which depends on a set of model parameters. The model parameters are divided into known welding parameters and unknown heat source parameters. As illustrated in figure 1 the unknown heat source parameters are identified iteratively solving the inverse heat conduction problem.

The transient temperature field during welding is calculated numerically in the present work using the finite element method (FEM). Within the calculation the field equation of transient heat conduction (eq. (1)) is solved.

$$\frac{\partial T}{\partial t} = \frac{\lambda}{c\rho}\left(\frac{\partial^2 T}{\partial x^2} + \frac{\partial^2 T}{\partial y^2} + \frac{\partial^2 T}{\partial z^2}\right) + \frac{1}{c\rho}q^{vol} \qquad (1)$$

Here, T is the temperature, t stands for time and x, y, z are coordinates fixed in space. The thermal conductivity λ, the specific heat capacity c and the density ρ are temperature dependent. On the right hand side of eq. (1) the heat input during welding is considered with the power density q^{vol} being a function of the heat input Q due to the welding arc and the coordinates x', y', z' moving together with the heat source (cp. figure 2). Eq. (1) is solved within a limited body. The corresponding thermal initial - boundary value problem is illustrated in figure 2 exemplarily for a single-pass surfacing. Details to the relevant initial and boundary conditions are given there as well. An initial temperature T_0 is prescribed for the whole calculation domain at time $t = 0$. The heat transfer by convection and radiation from surface S to ambient is considered by defining the fluxes $\overline{q}^{con.}$ and $\overline{q}^{rad.}$.

$$\overline{q}^{con.} = \alpha\left(T_S - T_{amb.}\right) \qquad (2a)$$

$$\overline{q}^{rad.} = \varepsilon \cdot \sigma_B\left(T_S^4 - T_{amb.}^4\right) \qquad (2b)$$
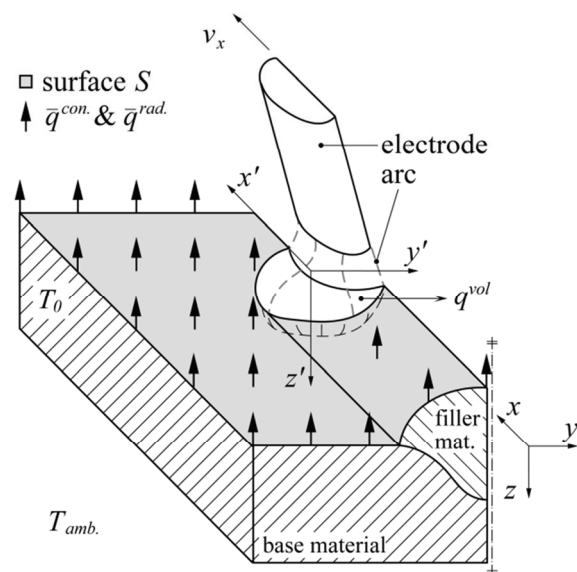
Fig. 2. *Thermal initial - boundary value problem during single-pass surfacing*

Here, α and ε are the heat transfer coefficient and the emissivity. The variables T_S and $T_{amb.}$ refer to the temperature at the surface S and ambient. The Boltzmann constant is $\sigma_B = 5.6704\cdot10^{-10}$ W·m⁻²·K⁻⁴. Numerical values for α, ε and $T_{amb.}$ are given in section 4.

The power density q^{vol} is determined within the double-ellipsoidal heat source model by Goldak and Akhlaghi (2005) as given in eq. (3).

$$q^{vol}(x',y',z',t) = \frac{6\sqrt{3}Q^{FEM}}{\pi\sqrt{\pi}\,y_q z_q} \begin{cases} \frac{f^f}{x_{qf}}\exp\left[-3\frac{x'^2}{x_{qf}^2} - 3\frac{y'^2}{y_q^2} - 3\frac{z'^2}{z_q^2}\right] & \text{if } x' > 0 \\ \frac{f^r}{x_{qr}}\exp\left[-3\frac{x'^2}{x_{qr}^2} - 3\frac{y'^2}{y_q^2} - 3\frac{z'^2}{z_q^2}\right] & \text{if } x' < 0 \end{cases}$$

$$\text{with } f^f + f^r = 2 \text{ and}$$
$$f^i = 2x_{qi}/[x_{qf}+x_{qr}] \quad (3)$$
$$(i = f \text{ or } r)$$

The ellipsoid is divided into a front part (index f) and a rear part (index r). Therefore, the heat input is divided by the weighting factors f^f and f^r. The shape and size of the double ellipsoid are defined by the parameters $x_{qf/r}$, y_q and z_q, see figure 3. They result from calibrating the simulation with experimental temperature measurements. In order to simplify the calibration the arc efficiency is assumed to be $\eta_{arc} = 65\%$. This value is extracted from the given range for manual metal arc welding, Radaj (1993). The power density q^{vol} depends on several model parameters which are combined in the heat input Q^{FEM}. The latter is calculated according to eq. (4). Here, the two parameters f_1 and f_2 make sure that the desired heat input Q is prescribed correctly within the power density q^{vol}. Integrating q^{vol} over the ellipsoid volume gives only 88,84% of the desired heat input Q (cp. Lindgren (2007)). Therefore, Q is multiplied by the scaling factor $f_1 = 1/0,8884$. Otherwise the solution of the volume integral depends on the mesh size of the finite element model. The mesh dependency is taken into account using the scaling factor f_2. The welding parameters I_{rms} (welding current) and U_{rms} (welding voltage) are measured during the process.

$$Q^{FEM} = f_1 \cdot f_2 \cdot Q \text{ with } Q = \eta_{arc} \cdot U_{rms} \cdot I_{rms} \quad (4)$$

Based on eq. (3) the Goldak heat source defines the heat input which is necessary to heat and melt the base material (cp. upper part of figure 3). In order to model multi-pass welding efficiently the source ellipsoid is projected onto the bead contour consisting of base- and filler material. Due to the projection the original convex heat source domain is transferred to a concave domain as can be seen in the cross-sectional view in figure 3.

This approach considers curved component surfaces and subjects heat to the filler material as well as to the base material. The surface contour is described by a function $f(y)$, which e.g. for the first elliptical layer has the form $f(y) = -\sqrt{\left(1-\frac{y^2}{a^2}\right)\cdot b^2}$ (cp. section 4). The parameters a and b define the width of the first layer ($a = 4.3$ mm) and its height ($b = 2.9$ mm). The comoving coordinates of the heat source (x', y', z') are transformed to coordinates (x, y, z) fixed to the weld specimen by eq. (5), where v_x denotes the welding velocity.

$$x' = x - t\cdot v_x; \; y' = y; \; z' = |f(y)| + z \quad (5)$$

It is possible to adapt this procedure to multi-pass surfacing and edge fillet welds as well. The modified Goldak heat source is implemented in to ABAQUS by a user subroutine, as explained by Kuźniar et al. (2011).
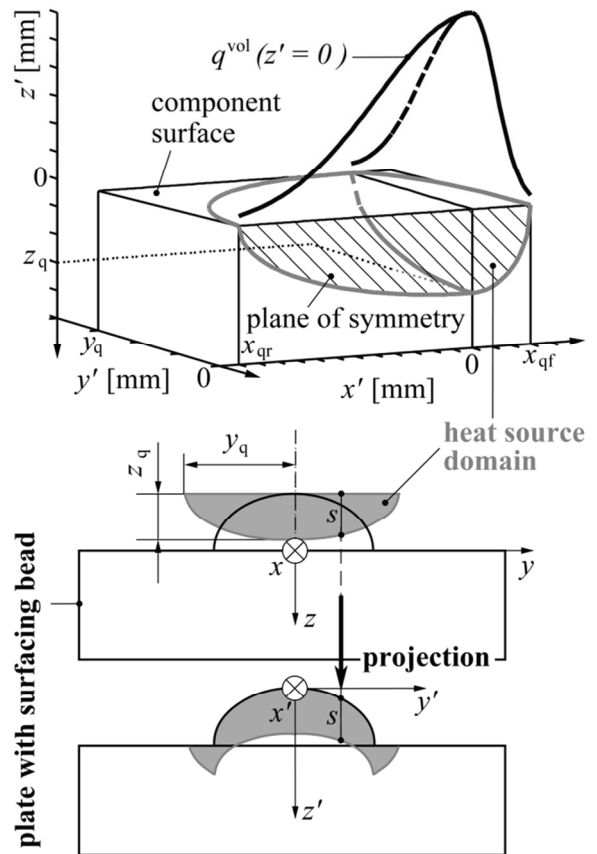

Fig. 3. *Application of the Goldak heat source*

During manual metal arc welding filler material covered with slag is added to the component surface following the moving electrode. The finite element model initially includes the whole geometry of the weld seam. However, the adding of filler metal and slag is modelled by two different material definitions. Distinguishing between added material (active) and non-added material (inactive) as shown in figure 4. In the thermal analysis a material point of the filler metal is activated as soon as the front of the heat source ($x' = x_{qf}$) reaches the material point. The initial temperature of the filler metal is equal to ambient temperature $T_0 = T_{amb.} = 25^oC$. In the activated state the filler material is molten due to the heat input from the heat source. Heating of the slag is not taken into account. The slag is activated in the centre of the heat source ($x' = 0$) and its initial temperature is assumed to be $T_0 = 1500^oC$.

minal of the welding machine. Natural convection can be assumed all around the specimen due to the design of the suspension. Basic electrodes (E 42 4B 42 H5) are used with a core wire diameter of 3.2 mm. Welding is executed with a positive poled electrode (DC). The arc length is approximately 3.2 mm, which corresponds to the core wire diameter. The slag resulting from the electrode burn-off is removed from each layer after welding. The welding process parameters (I, U, t^{weld}) are measured online by the process sensor HKS P 1000. The temperature distribution during welding and over the period of cooling is measured via thermocouples. The thermocouples are arranged in a row under the welding line as illustrated in figure 5. With this arrangement it is possible to check if the temperature field is quasi stationary. The measurement loops are placed at a distance of 4 mm to the specimens' top surface
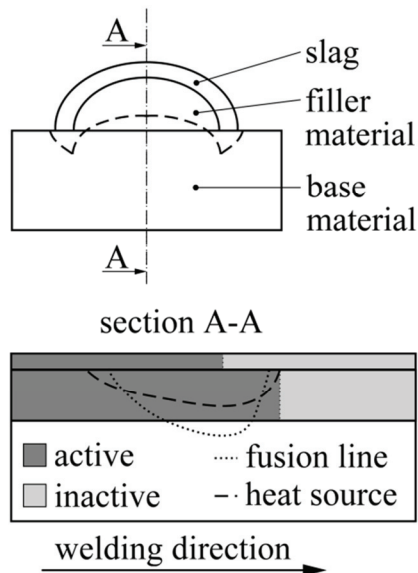

Fig. 4. Activation of filler material and slag

3. EXPERIMENTAL APPROACH

The welding experiment deals with a double-pass surfacing. In order to calibrate the thermal simulation the following information are taken from the experiment: temperature distribution, welding parameters, bead shape, and macrosections.

3.1. Experimental set-up

The double-pass surfacing is carried out on a plate (S355J2G3) with the dimensions of 250 mm x 175 mm x 10 mm. Figure 5 provides an overview of the experimental set-up. The plate is located in a suspension which is connected to the ground ter-
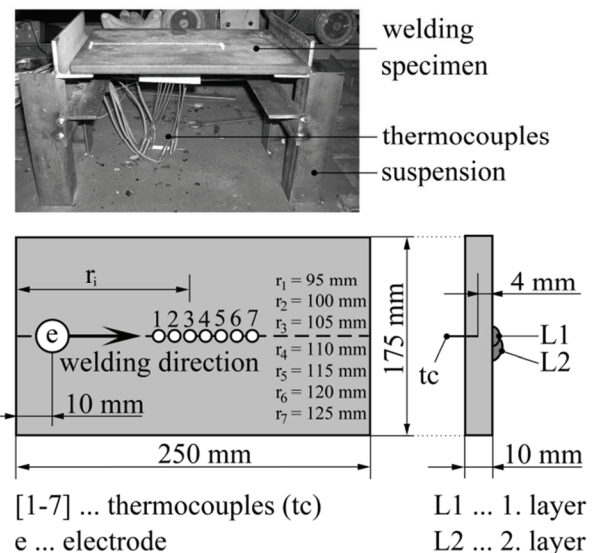

Fig. 5. Experimental set-up for the surfacing

within the heat affected zone (HAZ) of the first layer. Macrosections are prepared from the surfacing at position $r_1 = 95$ mm (thermocouple 1) and $r_4 = 110$ mm (thermocouple 4) in order to post process the bead contour, the fusion line and the HAZ.

3.2. Detection of process parameters

Figure 6 illustrates the welded seam in connection with the weld seam dimensions, the welding parameters and the macrosections. Within a macrosection the dotted line marks the fusion line and the dashed line marks the outer edge of the HAZ. Both lines are relevant for validating the simulated temperature field. At the fusion line the temperature range is between liquidus (T_{liq}) and solidus tempera-

ture (T_{sol}). For the plate material S355J2G3 the temperature range T_{liq} = 1520°C and T_{sol} = 1420°C can be found in Spur and Stöferle (1987). It is assumed that the temperature range at the outer bound of the HAZ is between A_{c1} and A_{c3}. According to Seyffarth et al. (1992) this temperature range is given for S355J2G3 with A_{c1} = 720°C and A_{c3} = 880°C.
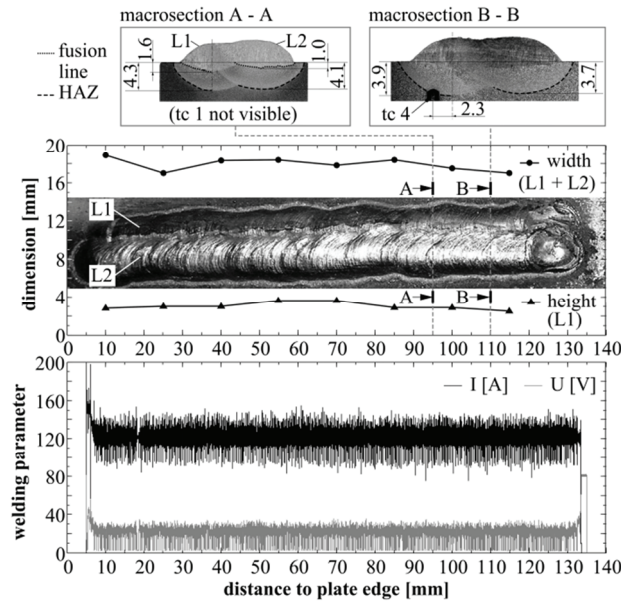

Fig. 6. *Macrosections and process parameters for the double-pass surfacing (dimensions in mm, tc = thermocouple, L1 = first layer, L2 = second layer)*

The weld seam dimensions are measured along the weld line as shown in figure 6. The height of the first layer is between 2.5 mm and 3.6 mm and the width of both layers between 17.0 mm and 18.9 mm. The deviations result from the manual electrode handling. The average values of the weld seam dimensions are used in the simulation (height of first layer equals 3.0 mm / height of second layer equals 3.3 mm / width of both layers equals 17.9 mm). The manual electrode handling influences the dimensions of the fusion line and the HAZ as well. Therefore, the fusion lines and HAZs obtained from the macrosection A and B are not identical (cp. figure 6). The weld line deviates from the desired line about 2.3 mm at macrosection B (cp. marked thermocouple 4 in figure 6).

Table 1 provides an overview of the welding process data. The welding machine operates with a current of about 120 A. The rms-value of both the welding current and voltage is listed in table 1. The progress of the welding parameters along the weld line is shown in figure 6. The steady state range between 10 mm and 130 mm (distance to the plate edge) is taken into account

to calculate the rms-values of welding current and voltage.

Table 1. *Welding parameters for the surfacing*

L	I_{rms} [A]	U_{rms} [V]	P [W]	t^{weld} [s]	s [mm]	v [mm/s]	E [Ws/mm]	t^{C} [s]
1	121.7	22.9	2792.3	78.8	130	1.65	1692.5	47
2	121.7	22.5	2743.6	75.3	131	1.74	1577.0	76
L – layer, s – weld length, E = $U_{rms} \cdot I_{rms}/v$ (energy per unit length), t^{C} – cooling time								

4. FE-MODEL

The thermal field is computed for the double-pass surfacing. The used FE-model includes the plate as well as both welding beads. Each welding layer is calculated with a separate FE-model. An overview about the FE-model and the selected thermal boundary conditions is given in figure 7. The bead shape as determined from the macrosections is approximated with elliptical segments as shown in figure 8. The FE-mesh consists of 8-node linear brick elements (thermal analysis: DC3D8 in ABAQUS). Close to the welding bead a small element size of 0.5 mm x 0.5 mm perpendicular to the welding direction and 1 mm in welding direction is chosen. This fine mesh is necessary for an accurate approximation of the high temperature gradients in this region.
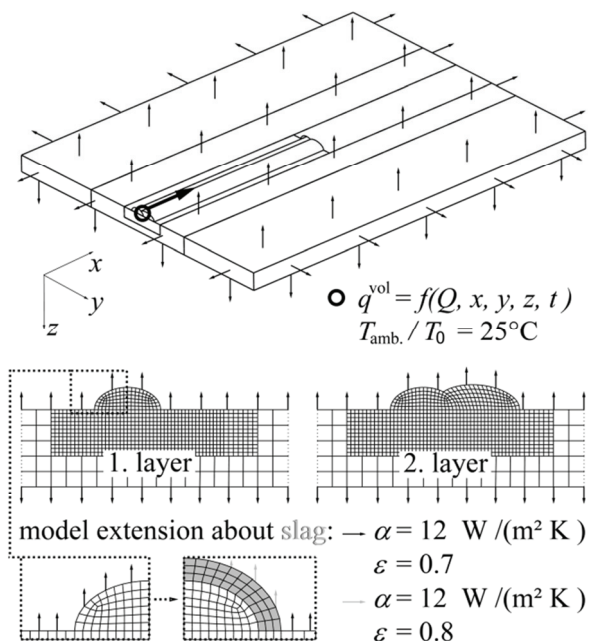

Fig. 7. *ABAQUS FE-model for double-pass surfacing with thermal boundary conditions*

The heat transfer by natural convection is taken into account all around the plate with a heat transfer coefficient $\alpha = 12$ W/(m^{2}K) (air convection according to Baehr and Stephan (2011)). The heat transfer by radiation is considered as well all around the plate with the emissivity $\varepsilon = 0.7$ (for oxidized steel surfaces according to Baehr and Stephan (2011)). The thermal boundary conditions are defined separately for each layer as illustrated in figure 7. The effect of the slag on the welding temperature field is analysed for the first layer within an extended FE-model (cp. figure 7). According to the rough surface of the slag the increased emissivity $\varepsilon = 0.8$ (for coal according to Baehr and Stephan (2011)) is considered.

The heat input due to welding arc is modeled by the Goldak heat source q^{vol} as described in section 2. Figure 8 illustrates the heat source domain for the double-pass surfacing. The heat source parameters $x_{qf/r}$, y_q and z_q which result from calibrating the simulation with temperature measurements are listed in figure 8.
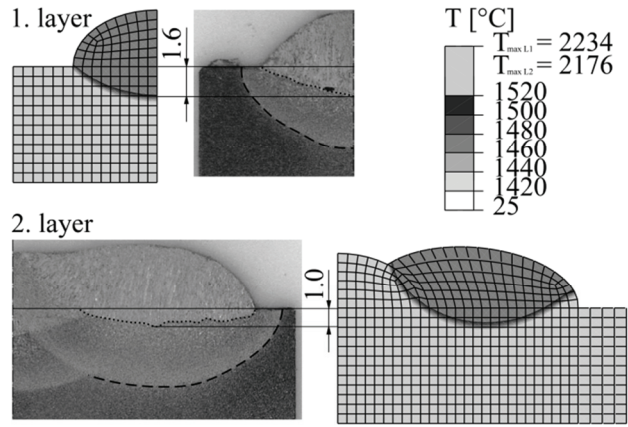

Fig. 9. *Matching for the fusion line (macrosection A, cp. figure 6)*

Analogously to the previous approach figure 10 illustrates the matching for the HAZ. The calculated temperature range between A_{c1} and A_{c3} matches the outer edge of the HAZ from the macrosection for the first layer as well as for the second layer.

The thermocouple measurement loops 1 and 4 are selected to evaluate the computed time-temperature curves, as shown in figure 11. In order to compare measurement and computational results
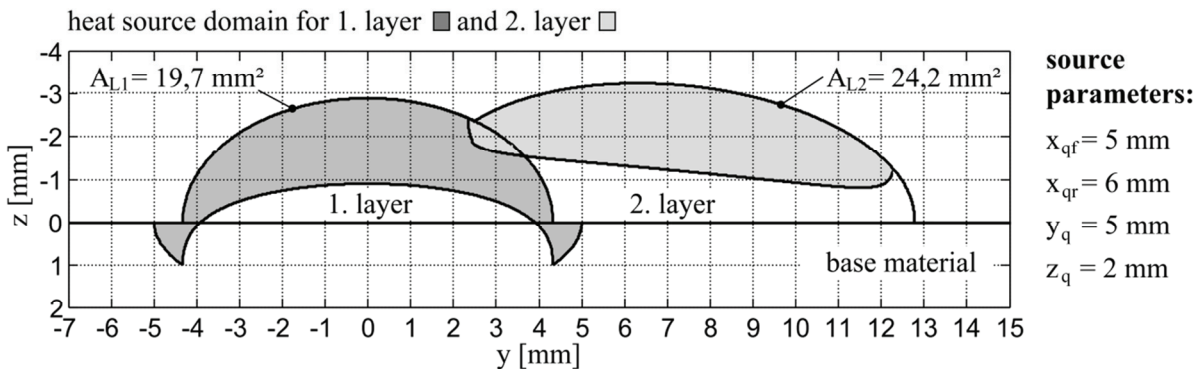

Fig. 8. *Bead shape and heat source domain for the double-pass surfacing ($A_{L1/2}$ – surface area of the 1. / 2. layer)*

5. COMPUTATIONAL RESULTS

The thermal field is computed with the welding parameters given in table 1, the arc efficiency $\eta_{arc} = 65\%$ and the heat source dimensions illustrated in figure 8. In order to validate the calculation results with the macrosection A the temperature field is plotted for the corresponding cross section in figure 9 and 10. The computed fusion line of the first layer matches the macrosection very well, as shown in figure 9. The simulated weld bead penetration of the second layer is in agreement with the macrosection, but the weld bead shape deviates slightly from the macrosection.

the calculated temperatures are averaged over the marked mesh nodes in figure 10. The selected mesh nodes represent the cone point of the thermocouples (cp. figure 6 macrosection B). Therefore, the real position of thermocouple 4 (cp. figure 6 macrosection B) is regarded. Thermocouple 1 is assumed to be located centrally below the first layer. The computational results are in good agreement with the measurement. The calculated local peak temperatures deviate from measurement loop 1 by 5.8% maximum and from measurement loop 4 by 17.2% maximum according to table 2.
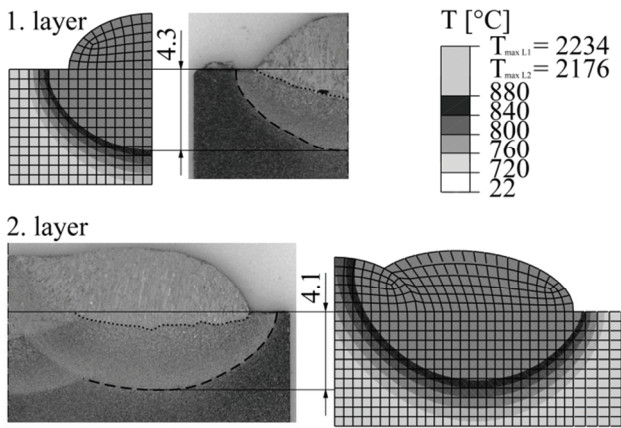
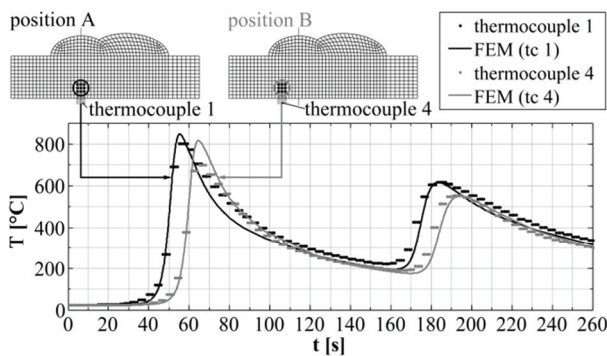**Fig. 10.** *Matching for the HAZ (macrosection A, cp. figure 6)*

Fig. 11. *Matching for the time-temperature curves of measurement loop 1 and 4*

Table 2. *Measured and calculated local peak temperatures for the first (L1) and second layer (L2) (cp. figure 11)*

	tc 1 L1	tc 1 L2	tc 4 L1	tc 4 L2
measurement	801.8°C	616.7°C	697.4°C	531.9°C
calculation	848.5°C	616.0°C	817.1°C	550.8°C
deviation	+5.8 %	-0.1 %	+17.2 %	+3.6 %
deviation – deviation of calculated from measured values				

The cooling curve of the first and second layer at measurement loop 4 is predicted in good agreement with the experimental data. However loop 1 cools down faster in the simulation then in the experiment. The measured cooling time t_{85} between 800°C and 500°C amounts $t_{85} = 25.5$ s. The predicted t_{85}-time is 36.5% lower ($t_{85} = 16.2$ s).

5.1. Influence of the slag

The influence of the slag is analysed according to the deviating cooling times between simulation and experiment at measurement loop 1. The slag is included within an extended FE-model for the first layer as mentioned in chapter 4.

Figure 12 compares the computational results of the FE-model without slag (reference) to the FE-model with slag included. The molten zone and the HAZ are slightly enlarged due to the slag in comparison with the slag-free simulation. The main effect of the slag can be seen in connection with the thermo cycles. The cooling is slowed down, due to the slag. Concerning measurement loop 1 the deviation of the computed and measured t_{85}-time is reduced to 25.5% ($t_{85\ with\ slag} = 19.0$ s / $t_{85\ measurement} = 25.5$ s). The peak temperatures of the thermo cycles are not influenced due to the slag.
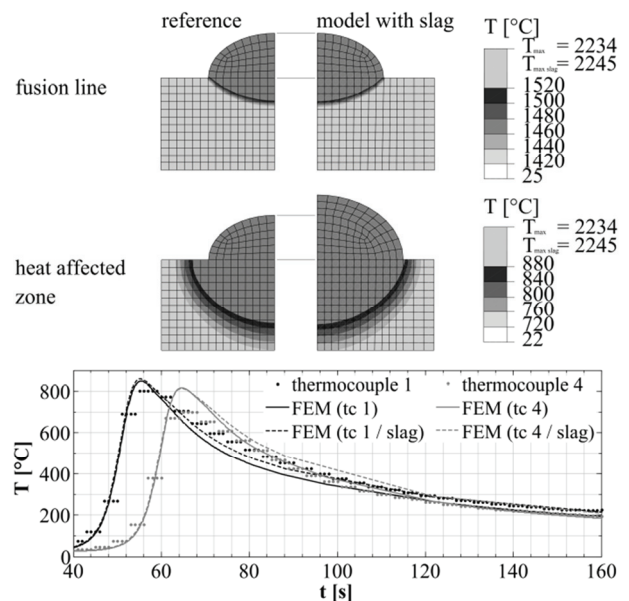

Fig. 12. *Influence of the slag on the first layer*

5.2. Discussion

In the following the source dimension parameters and the deviation between experimental and computational results are discussed.

The parameters $x_{qf/r}$, y_q and z_q are obtained from calibrating the heat source model with the temperature measurement within the scope of the first layer. The calibrated heat source predicts the welding temperature field for the first layer in good agreement with the experiment. According to the work of Goldak and Akhlaghi (2005) the heat source dimensions are related to the dimensions of the weld pool. The heat source width ($y_q = 5$ mm) is equal to the weld pool width of layer one within the current calibration (cp. figure 7). The heat source depth (z_q) is not equal to the penetration depth as required by Goldak and Akhlaghi (2005). This deviation is caused by projecting the source ellipsoid onto the bead contour. The computed fusion line fits the macrosection if z_q equals two thirds of the bead height. The size of the

liquefied region can additionally be scaled by the arc efficiency η_{arc}. Doing so, the calculated peak temperatures of the thermo cycles are influenced as well, probably giving a better representation of the measured maximum temperatures. However, η_{arc} is not used as scaling factor in this work, since the applied value of $\eta_{arc} = 65\%$ is already at the lower limit of the given range for manual metal arc welding according to Radaj (1993).

Both layers are simulated with the same source dimension parameters due to the identical welding parameters I_{rms}, U_{rms} and v (cp. table 1). The computed fusion line for the second layer deviates from the macrosection. The fusion line is to narrow, so that the filler material is melt on only incompletely. Thereby the difference between the cross-sectional areas of the first and second welding bead has to be taken into account. The cross-sectional area of the second layer ($A_{L2} = 24.2$ mm^2) is 22.8% larger than the area of the first layer ($A_{L1} = 19.7$ mm^2). In order to improve the matching the heat source parameters should be adjusted separately for each layer.

On the experimental part the measured temperature field is influenced by the electrode motion and the slag. The welding line deviates from the desired path and the welding parameters vary. The effects due to the electrode motion are simplified using averaged welding parameters (I_{rms}, U_{rms} and v) and an idealized welding path. The path deviation at thermocouple loop 4 is detected from the macrosection (cp. in figure 6) and is considered during post processing. In order to evaluate the accuracy of the thermocouple measurements the following points should be taken into account. The measured peak temperatures strongly depend on the location of the measurement loop, due to the high temperature gradients in the measuring zone. Potential measuring errors decrease regarding the cooling curves, because temperature gradients decrease as well. Therefore, the validation of computed thermo cycles with thermocouple measurements should focus on the cooling behaviour. Concerning the FE-model without the slag the computed and measured cooling curves are in acceptable agreement. The analysis of the slag influence shows, that a realistic cooling behaviour is simulated incorporating the slag in the FE-model.

6. CONCLUSION

Multi-pass welding is examined by means of experiment and simulation in order to assess welded joints. A modeling concept for multi-pass welding is implemented in the FE-code ABAQUS and is tested for a multi-pass surfacing. The welding temperature field is computed using a modified Goldak heat source, which is adapted to the multi-pass process. The modified heat source model is calibrated to the first layer of a double pass surfacing and provides an acceptable representation of the temperature field for both layers. The influence of the slag on the welding temperature field is analysed for the first welding layer. The modeled slag decelerates the cooling in the HAZ and a realistic cooling behaviour is simulated.

With respect to the further procedure the welding stresses and the microstructure distribution has to be computed using the obtained temperature field. Experiment and simulation has to be extended to edge fillet welds. Validating the computational results with thermocouple measurements and macrosections is inevitable. In order to accelerate the model calibration a correlation has to be found for welding parameters and the parameters of the heat source model. This correlation should be analysed within the scope of a parameter study.

REFERENCES

Baehr, H. D., Stephan, K., 2011, *Heat and Mass Transfer*, Springer-Verlag, Berlin.

Deng, D., Murakawa, H., 2006, Numerical simulation of temperature field and residual stress in multi-pass welds in stainless steel pipe and comparison with experimental measurements, *Computational Material Science*, 37, 269-277.

Goldak, J. A., Akhlaghi, M., 2005, *Computational welding mechanics*, Springer Science+Business Media Inc, Boston MA.

Kuźniar , A., Rygiel, P., Dudek, S., Gnot, A., Gancarczyk, T., Perzyński, K., 2011, Numerical model of a TIG welding process for the aviation industry, including analysis of the heat transfer, *Computer Methods in Material Science*, 11, 173-178.

Lindgren, L.-E., 2007, *Computational welding mechanics: Thermomechanical and microstructural simulations*, Woodhead Publishing Limited and CRC Press, Cambridge.

Pittner, A., Weiss, D., Schwenk, C., Rethmeier, M., 2011, Fast temperature field generation for welding simulation and reduction of experimental effort, *Welding in the World*, 55, 83-90.

Radaj, D., 1993, *Heat Effects of Welding*, Springer-Verlag, Berlin.

Radaj, D., 1999, *Welding Process Simulation: Fundamentals and Applications*, DVS Verlag, Düsseldorf (in German).

Sabapathy, P. N., Wahab, M. A., Painter, M. J., 2001, Numerical models of in-service welding of gas pipelines, *Journal of Materials Processing Technology*, 118, 14-21.

Seyffarth, P., Meyer, B., Scharff, A., 1992, *Großer Atlas Schweiß-ZTU-Schaubilder*, Deutscher Verlag für Schweißtechnik DVS-Verlag GmbH, Düsseldorf (in German).

COMPUTER METHODS IN MATERIALS SCIENCE

Spur, G., Stöferle, T., 1987, *Handbuch der Fertigungstechnik Band 4/2 Wärmebehandeln*, Carl Hanser Verlag, München (in German).

Weiss, D., Christensen, K. H., Kristensen, J. K. 2007, Algorithms for inverse analysis of heat deposition processes, *Mathematical Modelling of Weld Phenomena*, 8, 847-879.

DOŚWIADCZALNA I NUMERYCZNA ANALIZA SPAWANIA WIELOPRZEPUSTOWEGO

Streszczenie

Numeryczne symulacje są obecnie powszechnie używane jako narzędzie dla oceny połączeń spawanych i perspektywicznie umożliwią one optymalizację procesów spawania. Przewidywanie pola temperatury jest podstawą do oceny spawów. W artykule opisano obliczenia zmian temperatury w czasie wieloprzepustowego ręcznego spawania elektrycznego. Proces spawania modelowano metodą elementów skończonych wykorzystując program ABAQUS. Zaimplementowano podwójnie elipsoidalny model Goldaka dla źródła ciepła. Ten model uwzględnia wpływ metalu wypełniającego spaw oraz wpływ żużla. Aby zwiększyć efektywność symulacji źródło Goldaka jest rzutowane na zarys spawu. Wykonano doświadczenia spawania wieloprzepustowego, w których temperaturę mierzono za pomocą termopar. Wyniki doświadczeń posłużyły do weryfikacji opracowanego modelu. Otrzymano dobrą zodność pomiarów i obliczeń, a obliczone pole temperatury było także zgodne z obserwowanym na makrostrukturze kształtem strefy wpływu ciepła. Oceniono wpływ żużla na prędkość chłodzenia po spawaniu.